PNAS RESEARCH ARTICLE | BIOPHYSICS AND COMPUTATIONAL BIOLOGY OPEN ACCESS

Mechanism and cellular function of direct membrane binding by the ESCRT and ERES-associated Ca^{2+}-sensor ALG-2

Sankalp Shukla[a,b], Wei Chen[c], Shanlin Rao[d], Serim Yang[a], Chenxi Ou[a,b], Kevin P. Larsen[a,b], Gerhard Hummer[d,e], Phyllis I. Hanson[c], and James H. Hurley[a,b,f,1]

Edited by Axel Brunger, Stanford University, Stanford, CA; received October 17, 2023; accepted January 17, 2024

Apoptosis linked Gene-2 (ALG-2) is a multifunctional intracellular Ca^{2+} sensor and the archetypal member of the penta-EF hand protein family. ALG-2 functions in the repair of damage to both the plasma and lysosome membranes and in COPII-dependent budding at endoplasmic reticulum exit sites (ERES). In the presence of Ca^{2+}, ALG-2 binds to ESCRT-I and ALIX in membrane repair and to SEC31A at ERES. ALG-2 also binds directly to acidic membranes in the presence of Ca^{2+} by a combination of electrostatic and hydrophobic interactions. By combining giant unilamellar vesicle-based experiments and molecular dynamics simulations, we show that charge-reversed mutants of ALG-2 at these locations disrupt membrane recruitment. ALG-2 membrane binding mutants have reduced or abrogated ERES localization in response to Thapsigargin-induced Ca^{2+} release but still localize to lysosomes following lysosomal Ca^{2+} release. In vitro reconstitution shows that the ALG-2 membrane-binding defect can be rescued by binding to ESCRT-I. These data thus reveal the nature of direct Ca^{2+}-dependent membrane binding and its interplay with Ca^{2+}-dependent protein binding in the cellular functions of ALG-2.

ESCRT | membrane repair | calcium-binding protein | reconstitution | lysosome

Significance

Apoptosis linked Gene-2 (ALG-2) transduces Ca^{2+} signals to recruit proteins to the plasma membrane, lysosomes, and endoplasmic reticulum (ER) exit sites in many biological processes. The mechanism whereby ALG-2 interprets the Ca^{2+} signal for protein–protein interactions is well understood, but Ca^{2+} modulation of membrane binding is not. Here, we show how Ca^{2+} controls ALG-2 membrane binding. The presence of Ca^{2+} neutralizes electrostatic repulsion between apo-ALG-2 and acidic phospholipid membranes to allow membrane engagement by a surface that we characterize in the study.

Apoptosis-linked gene-2 (ALG-2) plays a central role in regulating various cellular processes, including plasma membrane and lysosome repair and vesicle budding at endoplasmic reticulum exit sites (ERES) (1). In the endosomal sorting complex required for transport (ESCRT) pathway (2, 3), ALG-2 senses Ca^{2+} released into the cytosol by plasma (4) and lysosome membrane damage (5), triggering recruitment of repair factors. ALG-2 also mediates effects of Ca^{2+} released by TRPML1 at lysosomes (6). At ERES, ALG-2 works with another penta-EF hand protein, PEF1, to regulate CUL3 and KLHL12-dependent ubiquitylation of COPII (7). Interest in the lysosome repair pathway, in particular, has intensified following recent discoveries of the role of cholesterol and ER-lysosome contact sites in repair (8, 9). Moreover, lysosome repair by the ESCRT machinery has been implicated in preventing the transmission of prion-like tau aggregates involved in Alzheimer's disease (10).

ALG-2 consists of five repeated EF-hand motifs and belongs to the penta-EF-hand (PEF) family (1). ALG-2 contains eight α-helices and forms dimers through the pairing of EF5 (11). The binding of ALG-2 to Ca^{2+} induces conformational changes that facilitate its interaction with proline-rich segments of its targets, of which the best known are the ESCRT proteins ALIX and TSG101 and the COPII subunit SEC31A (12–14). ESCRT-I and ALIX share the same binding site (15), while SEC31A binds at a distinct site (14).

Despite that all of the above-mentioned protein–protein interactions occur in the context of membranes, and many other families of Ca^{2+}-binding proteins interact directly with membranes (16–19), there has been little investigation of the role of the membrane itself in the recruitment functions of ALG-2. In the course of reconstituting Ca^{2+}- and ALG-2-dependent recruitment of ESCRTs to membranes (20), we noticed that ALG-2 had an intrinsic ability to bind acidic membranes in a Ca^{2+}-dependent manner even in the absence of ESCRTs. Building on this work, we investigated the mechanistic determinants and cellular function of this membrane-binding activity, and whether it had any physiological role.

To address these questions, we employed a three-pronged approach. First, we utilized a giant unilamellar vesicle (GUV) reconstitution system, which allowed us to leverage fluorescence microscopy in a precisely defined experimental setup. By designing ALG-2 mutants based on the X-ray crystal structure of ALG-2, we aimed to perturb its interaction with negatively charged membranes. Subsequently, molecular dynamics (MD) simulations were employed to more precisely identify the interactions responsible for the binding of ALG-2 to negatively charged membranes. Lastly, through live cell imaging techniques, we monitored the localization of ALG-2 membrane-binding mutants to ER-exit sites and lysosomes in response to Ca^{2+} release.

Author affiliations: [a]Department of Molecular and Cell Biology, University of California, Berkeley, CA 94720; [b]California Institute for Quantitative Biosciences, University of California, Berkeley, CA 94720; [c]Department of Biological Chemistry, University of Michigan School of Medicine, Ann Arbor, MI 48109; [d]Department of Theoretical Biophysics, Max Planck Institute of Biophysics, Frankfurt am Main 60438, Germany; [e]Institute of Biophysics, Goethe University Frankfurt, Frankfurt am Main 60438, Germany; and [f]Helen Wills Neuroscience Institute, University of California, Berkeley, CA 94720

Author contributions: S.S., G.H., P.I.H., and J.H.H. designed research; S.S., W.C., S.R., and S.Y. performed research; C.O. and K.P.L. contributed new reagents/analytic tools; S.S., W.C., S.R., and C.O. analyzed data; and S.S., S.R., G.H., P.I.H., and J.H.H. wrote the paper.

Competing interest statement: J.H.H. is a founder and consultant for Casma Therapeutics.

This article is a PNAS Direct Submission.

[1]To whom correspondence may be addressed. Email: jimhurley@berkeley.edu.

This article contains supporting information online at https://www.pnas.org/lookup/suppl/doi:10.1073/pnas.2318046121/-/DCSupplemental.

Published February 22, 2024.

Results

ALG-2 Mutants Abrogate Binding to Negatively Charged Membranes. Based on crystal structures of ALG-2 (11, 14, 15), we predicted two regions might contribute to the membrane binding of ALG-2 to negatively charged membranes. The first is a basic patch consisting of Arg34, Lys37, and Arg39, which are exposed such that they could bind to negatively charged membranes, and the second is the exposed hydrophobic sidechain of Trp57 (Fig. 1*A*). We hypothesized that the electrostatic interaction of the RKR motif with the negatively charged membrane might stabilize binding of ALG-2 to acidic membranes. Once the ALG-2 is in the vicinity of the membrane, the Trp57 residue likely embeds in the membrane, reinforcing the binding of ALG-2 to negatively charged membranes.

GUV membrane binding was tested for the point mutant W57E, the triple mutant R34E/K37E/R39E, and the double mutant R39E/W57E. All of these mutants were made in the background of an introduced Cys78 for fluorophore labeling at a location distal to the putative membrane binding face. Proteins were expressed at the same levels and behaved essentially the same in purification, consistent with a lack of gross changes in protein stability. The AlphaFold2 (AF2) (21) predicted model of R34E/K37E/R39E ALG-2 superimposed upon the crystal structure of des3-20 WT ALG-2 [Protein Data Bank (PDB—2ZN9)] resulted in a RMSD of 0.7 Å across the ordered backbone atoms from residues 24 to 188 (*SI Appendix*, Fig. S1). The lack of structural perturbation was expected and is consistent with the exterior location of the mutated sidechains. We incubated GUVs containing 30% 1,2-dioleoyl-sn-glycero-3-phospho-L-serine (DOPS) along with 69.5% 1,2-dioleoyl-sn-glycero-3-phosphocholine (DOPC) and 0.5% Atto 647 N dye-labeled 1,2-dioleoyl-sn-glycerol-3-phosphoethanolamine (Atto 647N DOPE) with WT ALG-2 and all its mutants (Atto 488; 200 nM) for 15 min in reaction buffer. On imaging, the WT ALG-2 formed puncta on the membrane as reported previously (20). The triple charge reversal mutant R34E/K37E/R39E ALG-2 abrogated the membrane binding of ALG-2.

Moreover, the double mutant, R39E/W57E ALG-2 with a mutation in the basic patch and of the hydrophobic residue and W57E ALG-2 single mutation of the hydrophobic residue were also sufficient to abrogate the binding of ALG-2 to the negatively charged membranes (Fig. 1 *B* and *C*). Previously, the N-terminal region of ALG-2 rich in alanine, glycine, and proline residues has been speculated to contribute to the membrane binding of ALG-2 (22). To test this, we generated the ΔN23 mutant of ALG-2 and did the same experiment with GUVs. We found that the ΔN23 mutant of ALG-2 still binds the negatively charged membranes similar to that of WT ALG-2 (*SI Appendix*, Fig. S2). Taken together, this points to a concerted membrane binding effort of ALG-2, whereby electrostatic interactions position the ALG-2 dimer close to the membrane and then the insertion of the tryptophan residue in the hydrophobic core of the bilayer membrane cements the ALG-2 dimer to the membrane.

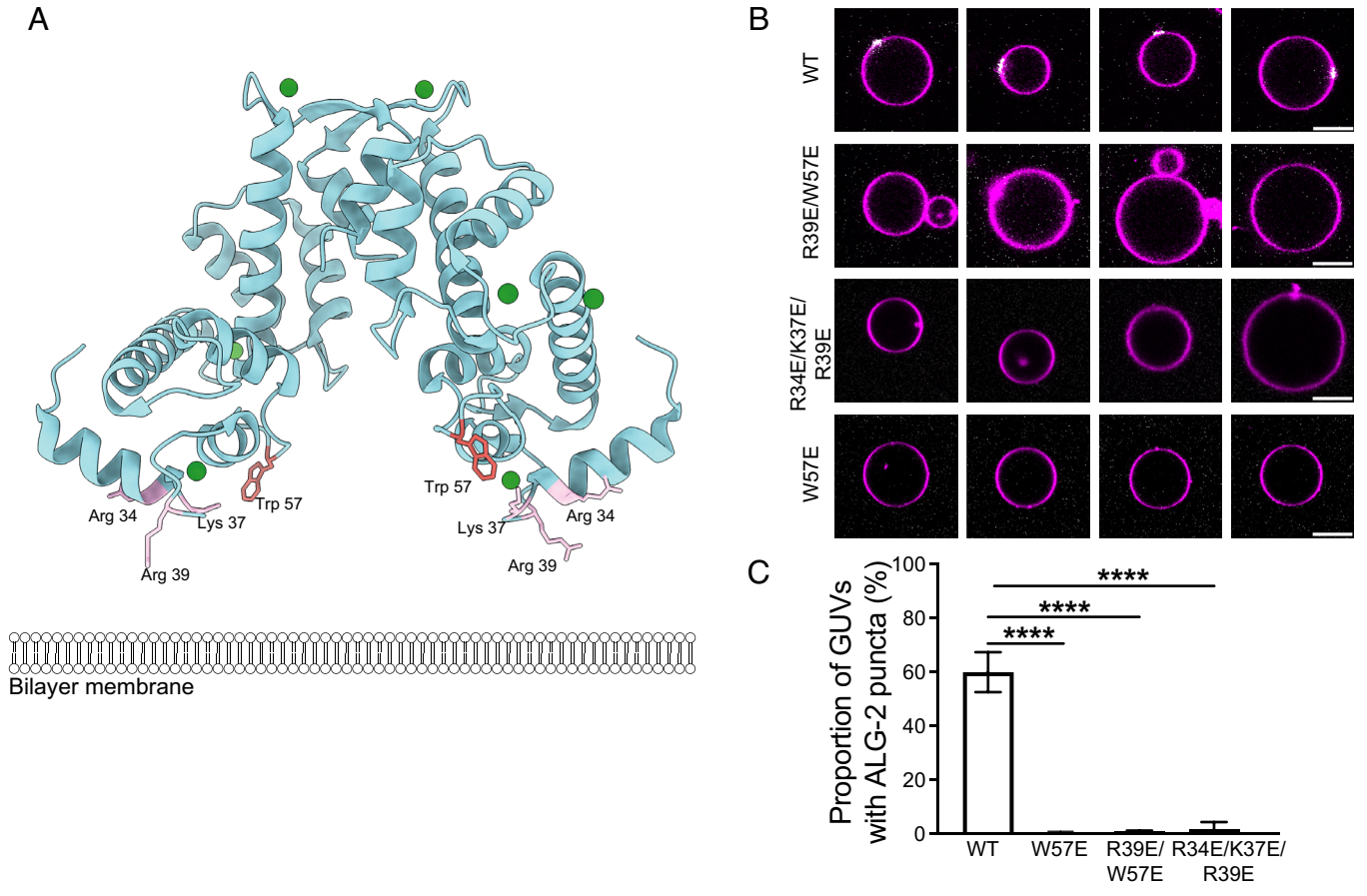

Fig. 1. ALG-2 mutants abrogate membrane binding to negatively charged membranes in a GUV-based assay. (*A*) Structure of Ca^{2+}-bound ALG-2 (PDB ID: 2ZN9) with residues Arg39 and Trp57 protruding toward a cartoon bilayer membrane. (*B*) ALG-2 A78C was fluorescently labeled with Atto 488 at the introduced Cys78. All mutants shown here were made in the A78C background. Wild-type and the indicated mutant ALG-2 proteins were incubated with 30% DOPS containing GUVs. (*C*) The proportion of GUVs that had at least one ALG-2 punctum (white) on their periphery (magenta) were plotted for fluorescently labeled WT ALG-2 (n = 1,388 GUVs), W57E (n = 395 GUVs), R34E/K37E/R39E ALG-2 (n = 741 GUVs), and R39E/W57E ALG-2 (n = 1,135). The data are shown as mean ± SD (vertical line). All results are from at least three independent experiments. $P \leq 0.0001$ (****). (Scale bar, 10 μm.)

A Triad of Basic Residues in EF1 Drives Electrostatic Interactions with Membrane. In all-atom MD simulations, Ca^{2+}-bound ALG-2 was observed to bind readily to negatively charged membranes consisting of 30% DOPS and 70% DOPC. A DOPC-only control for the Ca^{2+}-bound (holo) WT ALG-2 showed a statistically significant reduction in contacts compared to the 30% DOPS and 70% DOPS membranes (*SI Appendix*, Fig. S3*A*). Consistent with the MD results, ALG-2 did not bind to 100% DOPC GUVs (*SI Appendix*, Fig. S3*B*). These results are in line with our previous finding that negative charge density contributes to the calcium-dependent recruitment of ALG-2 to the membrane (20).

In the MD simulations, stable interactions were established mainly through EF1 (and to a lesser extent EF3) from each subunit of the dimer (Fig. 2*A* and *SI Appendix*, Fig. S4*A*). The three basic residues forming the RKR motif in EF1, namely Arg34, Lys37, and Arg39, examined above (Fig. 1*A*) initiated membrane association of ALG-2 through direct contacts with membrane lipids (Fig. 2*A*). Ca^{2+} ions bound to EF1 and EF3, partially encaged by their coordinating residues, were typically held at a distance of >0.5 nm from the nearest lipid atom (*SI Appendix*, Fig. S4*B*). Direct bridging of membrane lipids by Ca^{2+} did occur, albeit infrequently, with a total of six instances observed across six 2 μs simulation replicates. It is not possible, however, to rule out that more extensive sampling might reveal a more kinetically stable coordination complex. In each case, one or two phosphate oxygen atoms from a PS molecule replaced the Ca^{2+}-coordinating Asp/Glu oxygen(s) of the EF hand (*SI Appendix*, Fig. S4*C*). These direct coordination events (applying a distance cut-off of 0.35 nm) were generally short-lived (<2 ns in duration), with one longer interaction persisting for ~350 ns. No direct Ca^{2+} coordination occurred for PC lipids present in the membrane. Compared to the more active role of Ca^{2+} in mediating lipid interactions of C2 domain proteins (23, 24) and annexins (16), our simulation results suggest a mechanism of Ca^{2+}-dependent membrane binding principally through an electrostatic effect. The binding of Ca^{2+} ion switches the sign of the surface electrostatic potential around the EF hands from strongly negative to positive (Fig. 2*B*). Drawn to the negatively charged membrane (*SI Appendix*, Fig. S4*D*), holo ALG-2 then forms tight interactions with lipids via the RKR motif and a flanking aromatic residue. As might be expected, all three residues of the RKR motif show a strong preference for the negatively charged PS over PC (Fig. 2*C*). Among other residues that make frequent membrane contacts (including Asn30, Asn54, and Trp57), we observed the aromatic side chain of Trp57, in particular, inserted between lipid headgroups and interacted with the acyl core of the membrane (Fig. 2 *A* and *D*). These hydrophobic interactions of Trp57 likely help to anchor ALG-2 to the target membrane.

Mutations Reduce ALG-2 Membrane Binding in MD Simulations. In agreement with results from GUV experiments, the mutations W57E, R39E/W57E, and R34E/K37E/R39E in and near the RKR motif yielded dramatically reduced membrane recruitment in all-atom MD simulations. The R34E/K37E/R39E triple mutant, in particular, shows only transient membrane interactions at a level comparable to that of the apo protein (Fig. 2*E*).

ALG-2 Mutants Do Not Concentrate on ERES Following Calcium Efflux from the ER. ALG-2 is known to be recruited to ERES in response to local Ca^{2+} release (1, 13). ALG-2 binds COPII protein Sec31A at ERES and regulates ER to Golgi vesicle transport (25, 26). However, how ALG-2 associates with the ERES membrane is still unclear. To test whether requirements for ALG-2 binding to ERES parallel those of ALG-2 binding to GUVs, we expressed mCherry-ALG-2 WT or W57E in HeLa cells and examined responses to Thapsigargin (TG) treatment. TG induces passive ER Ca^{2+} release by inhibiting uptake into the ER via SERCA Ca^{2+}-ATPases and is known to trigger ALG-2 recruitment to ERES. As expected, ALG-2 WT formed puncta in response to TG that co-localized with Sec31A (Fig. 3*A*). In contrast, W57E mutant ALG-2 did not respond (Fig. 3*A*). To follow the dynamics of this ALG-2 recruitment, we used live-cell imaging and observed the expected rapid accumulation of WT but not W57E mCherry-ALG-2 puncta following TG treatment (Fig. 3 *B* and *C*). We also examined the response of R34E/K37E/R39E ALG-2 to TG and found that its response was reduced compared to that of WT (Fig. 3 *D* and *E*). These data show that all of the mutants that abrogate binding to GUVs in vitro also abrogate or at least reduce localization to ERES in response to ER Ca^{2+} release.

ALG-2 Mutants Respond Normally to Lysosomal Ca^{2+} Release. Locally triggered Ca^{2+} release is also reported to recruit ALG-2 to lysosomes (6) where it further engages ESCRT proteins (5, 20). To investigate the effect of the ALG-2 membrane binding mutations on its response to lysosomal Ca^{2+} release, we again performed live-cell imaging experiments. We transfected either mCherry-ALG-2 WT or ALG-2 mutants along with fluorescently tagged ESCRT-III protein IST1 into ALG-2 KO HeLa cells. We then used a TRPML1 agonist, ML-SA5, along with TG (27) and observed the expected recruitment of WT ALG-2 together with IST1 (Fig. 4*A*) and in the absence of IST1 (*SI Appendix*, Fig. S5). All ALG-2 mutants were similarly recruited along with IST1 to lysosomes at a level similar to that of WT ALG-2 (Fig. 4 *B*–*D*). This suggests that recruitment of ALG-2 mutants to lysosomal membranes and their association with ESCRT proteins is not affected by the ALG-2 membrane binding mutations.

ESCRT-I Rescues the Membrane Binding Ability of ALG-2 Mutants. The abrogation of ERES but not lysosome recruitment of the W57E ALG-2 mutant might be explained by the presence of ESCRT machinery in the latter case. We hypothesized that the Ca^{2+}-triggered recruitment of ESCRT machinery to lysosomal membrane could compensate for the decreased membrane binding of designed ALG-2 mutants.

To test compensation in vitro, we first incubated ESCRT-I (Cy3; 50 nM) and W57E ALG-2 (Atto 488; 200 nM) individually with 30% DOPS-containing membranes. We neither observed the recruitment of ESCRT-I nor W57E ALG-2 on the membrane individually (Fig. 5 *A*, *Top* and *Middle* row and 5*B*) under our experimental conditions. Next, we repeated the same experiment but with W57E ALG-2 (Atto 488; 200 nM) and ESCRT-I (Cy3; 50 nM) added together on the membrane. We observed clear colocalized puncta of ESCRT-I and W57E ALG-2 on the membrane (Fig. 5 *A*, *Bottom* row, 5 *B* and *C*). This suggests that the reduction in the membrane affinity of the W57E ALG-2 mutant is likely compensated by the ability of ESCRT-I itself to bind directly to membrane, for example, via the MVB12-associated β-prism (MABP) motif in ESCRT-I (28).

Discussion

While ALG-2 has long been understood to undergo Ca^{2+}-triggered protein–protein interactions, the role of Ca^{2+} in promoting its direct binding to acidic membranes has not been appreciated until recently. Our findings show that for ALG-2, the role of Ca^{2+} binding is to neutralize charge repulsion between the electronegative apo-ALG-2 protein and acidic membranes. Both the lysosome and ER membranes are negatively charged, as is the plasma

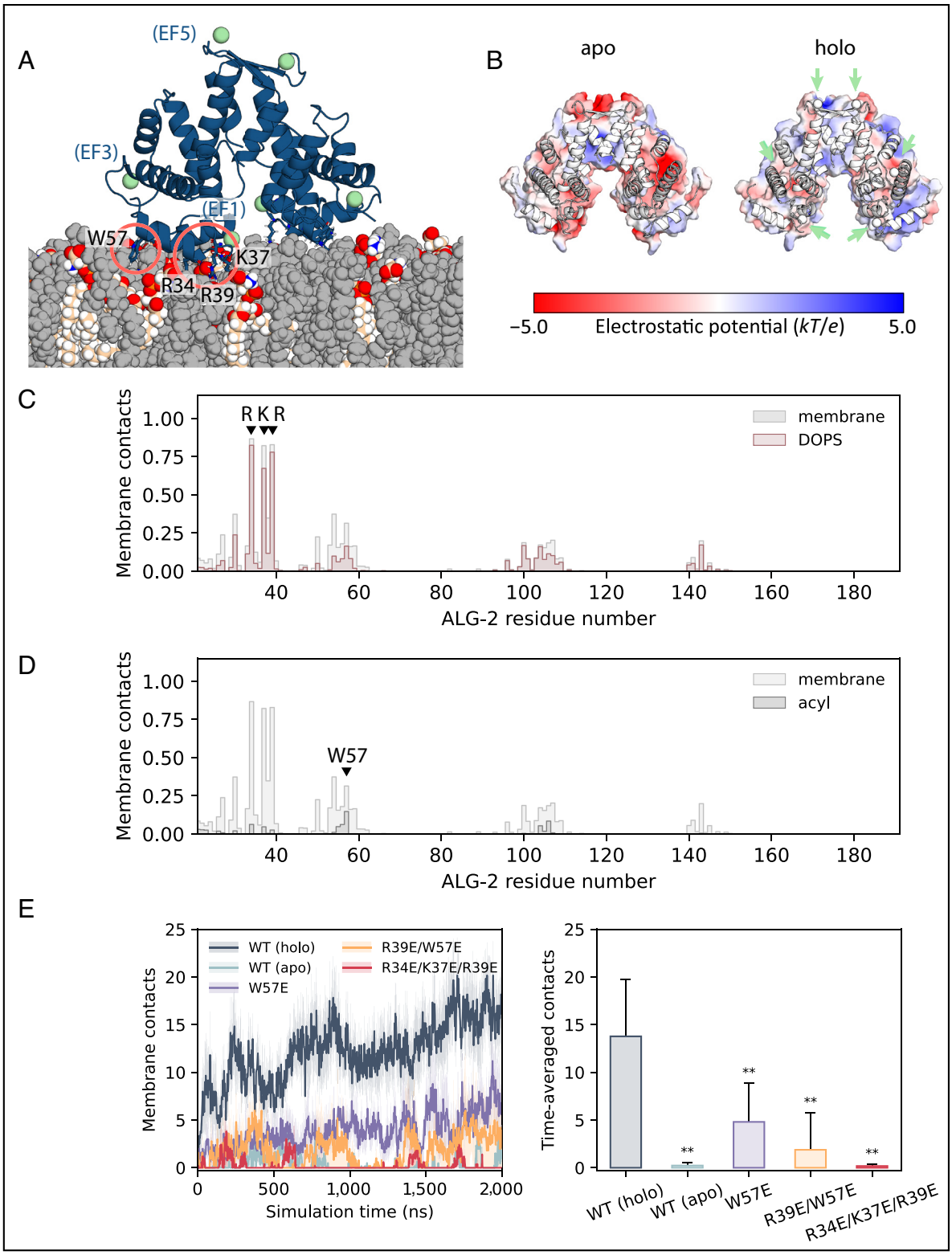

Fig. 2. MD simulations of ALG-2 membrane interactions. (*A*) Ribbon representation of Ca^{2+}-bound ALG-2 interacting with membrane lipids (spheres) upon spontaneous membrane binding during MD simulation. PS lipids are colored by atom type, with PC lipids in gray. Key membrane-interacting residues are highlighted. (*B*) Surface electrostatic potential of apo and Ca^{2+}-bound (holo) ALG-2. Positions of bound Ca^{2+} ions are indicated with green arrows. (*C*) Mean frequency of membrane and DOPS lipid contacts by each ALG-2 residue along the amino acid sequence, calculated as a percentage of analyzed frames from the final 1 μs of each of six 2 μs simulations, sampling at 2-ns intervals. (*D*) Mean frequency of membrane lipid and acyl tail contacts by each ALG-2 residue along the amino acid sequence. (*E*) Number of ALG-2 residues forming membrane contacts over the course of simulation replicates, comparing between the apo and Ca^{2+}-bound (holo) forms of wild-type (WT) ALG-2 and with mutants (holo). The mean (solid lines) and SE (semi-transparent shading) are plotted over time for six simulation replicates of WT ALG-2 and five of each mutant. Time-averaged membrane contacts and SD are also calculated across the final 1 μs of 2 μs simulation replicates of each structure. Statistically significant ($0.001 < P < 0.01$) reductions in membrane binding compared with the Ca^{2+}-bound WT protein, as assessed by one-tailed Student's *t* tests, are denoted by asterisks (**).

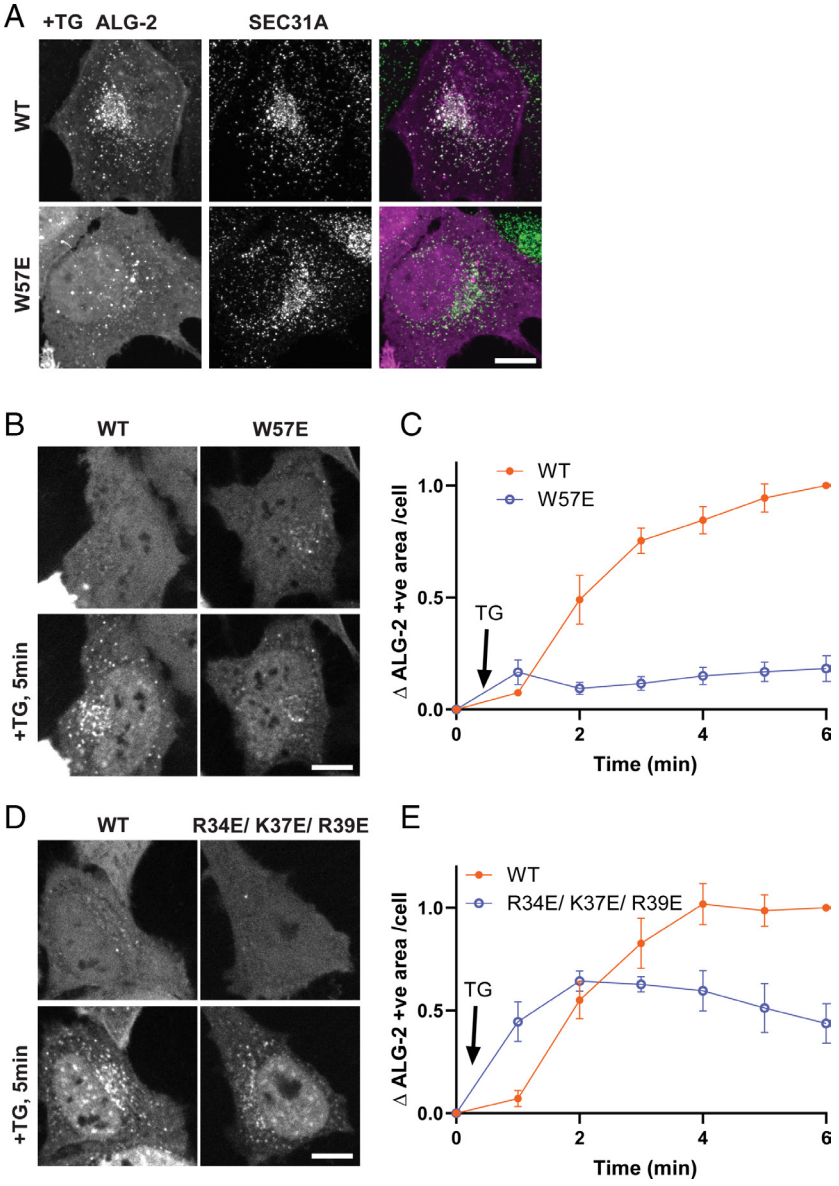

Fig. 3. ALG-2 mutants do not concentrate at ERES following TG-induced calcium release. (*A*) HeLa cells expressing mCherry-ALG-2 WT or W57E were treated with TG and stained for SEC31A. (*B*–*E*) Live imaging of HeLa cells expressing mCherry-ALG-2 WT, W57E, or R34E/ K37E/ R39E were imaged at 1 min intervals. (*B*) and (*D*) show cells before and after 5 min of TG treatment. (*C*) and (*E*) show mCherry-ALG-2 signal above threshold (mean ± SEM). Thirty-eight cells (WT) and 58 cells (W57E) from three experiments were analyzed in (*C*). Forty-nine cells (WT) and 60 cells (R34E/ K37E/ R39E) from three experiments were analyzed in (*E*). (Scale bar, 10 μm.)

membrane (29–31). This electrostatic neutralization mechanism contrasts to the direct Ca^{2+} bridging that has been characterized for annexins and C2 domains (16–19). In the case of ALG-2, direct Ca^{2+}-phospholipid coordination was briefly observed in simulation, but only rarely and for a few ns at a time. Thus, ALG-2 defines a mechanistically unique class of Ca^{2+}-stimulated membrane-binding protein.

ALG-2 is recruited both to lysosomal membrane and to ERES upon calcium efflux. A key distinction between these events is the absence ESCRT machinery at ERES. ALG-2 has three substrate binding pockets termed ALG-2 binding sites (ABS), ABS-1, -2, and -3. TSG101 and ALIX bind to pockets 1 and 2, whereas Sec31 binds to pocket 3. Trp 57 is at the edge of binding pocket 3, however, ALG-2 W57A has essentially normal binding to Sec31 in vitro (14). Furthermore, Arg 34, Lys 37, and Arg 39, which do have reduced ER recruitment, are located outside of pocket 3. The loss of ERES recruitment seen in these mutants can thus only reasonably be explained by the loss of membrane binding rather than a defect in Sec31 interaction.

ESCRT components, including ESCRT-I, have intrinsic membrane binding affinity. The MABP domain of the MVB12 subunit of ESCRT-I mediates its interaction with anionic lipids (28). Our previous study found that ESCRT-I, at a concentration of 50 nM, could be recruited only to 30% DOPS-containing membranes when WT ALG-2 is added. However, at relatively higher concentrations of 100 nM and 200 nM, ESCRT-I alone was sufficient to bind to 30% DOPS-containing membranes (20). Therefore, it is plausible that the downstream recruitment of ESCRT machinery assists the recruitment of ALG-2 to membranes in a positive feedback loop. The rescue of the membrane-binding ability of otherwise membrane non-binding ALG-2 mutants upon the addition of ESCRT-I in our GUV-based assay is consistent with this hypothesis. This supports a primary role for Ca^{2+}-stimulated ALG-2-ESCRT interaction, with a more secondary and ancillary role for Ca^{2+}-stimulated membrane binding in lysosome biology.

Materials and Methods

Materials. The lipids DOPC and DOPS (sodium salt) were obtained from Avanti Polar Lipids. Lipid fluorophore 1,2-Dioleoyl-sn-glycero-3-phosphoethanolamine labeled with Atto 647 (Atto 647 DOPE) was purchased from Sigma Aldrich. Thapsigargin was used at 2 μM (AC328570010, Thermo Scientific). HEPES,

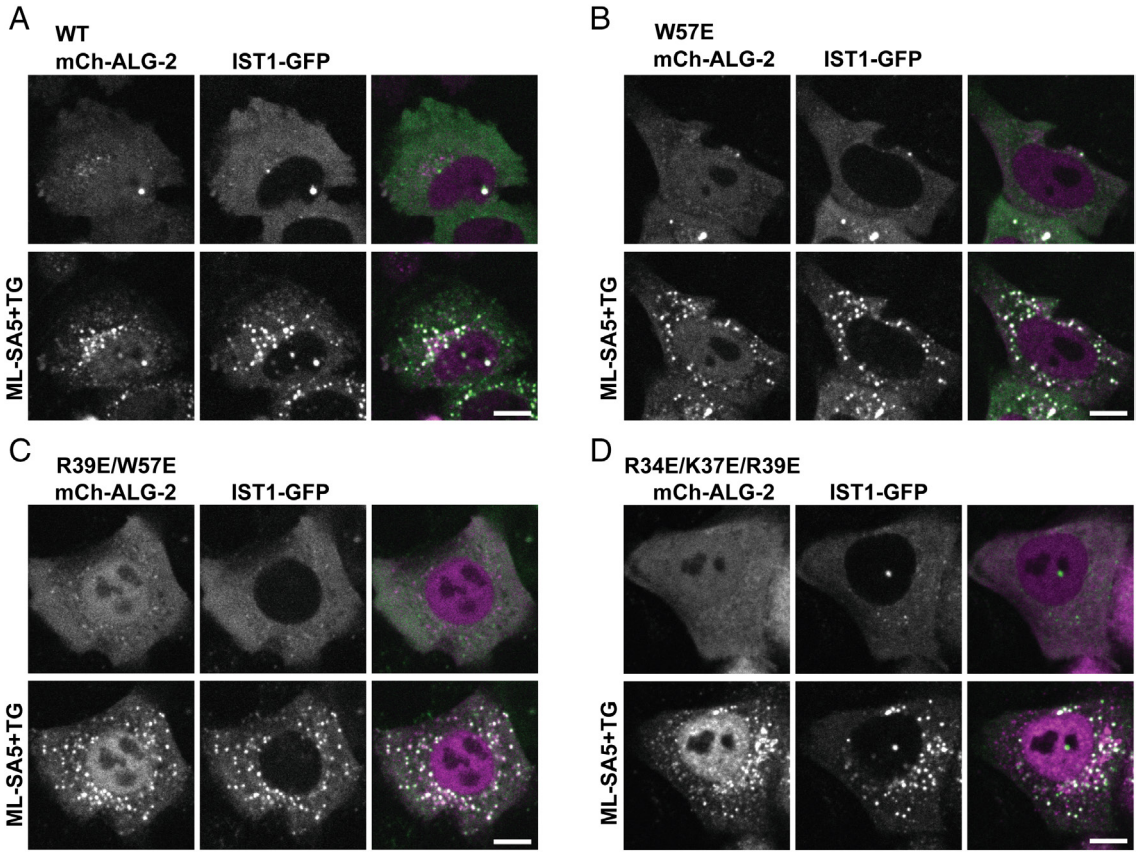

Fig. 4. ALG-2 mutants are recruited normally to lysosomes in response to triggered Ca^{2+} release. ALG-2 KO HeLa cells were co-transfected with IST1-mGFP and mCherry-ALG-2 WT (*A*), W57E (*B*), R39E/ W57E (*C*), or R34E/K37E/ R39E (*D*). Cells were imaged live before and 15 min after incubation with ML-SA5 and TG. (Scale bar, 10 μm.)

NaCl, EGTA, and fatty acid-free bovine albumin (BSA) were obtained from Fisher Scientific. All commercial reagents were used without further purification.

GUV Formation. GUVs containing DOPC (69.5 mol%), DOPS (30 mol%), and the lipid fluorophore Atto 647 DOPE (0.5 mol%) were prepared in 270 mOsm sucrose using PVA-gel hydration-based method as in Weinberger et al. (32). Briefly, lipids were mixed in chloroform at a total concentration of 1 mM. The 40 μL solution of the lipid mixture was spread on a 5% w/v PVA film dried on a 25 × 25 mm coverslip (VWR) and then put under vacuum for at least 2 h to form a dry lipid film. The dried lipid film was hydrated with 500 μL of 270 mOsm sucrose solution for 2 h at room temperature to produce GUV dispersion which was collected and stored in a 1.5-mL microcentrifuge tube.

Protein Purification. ALG-2 and all the mutants of ALG-2 (W57E; R34E/K39E/R39E; R39E/W57E; ΔN23) were purified based on the ALG-2 purification protocol described in McGourty et al. (7). Briefly, N-terminal 6x His tagged ALG-2 is expressed in *Escherichia coli* BL21 (DE3) cells in LB medium supplemented with kanamycin (50 μg/mL), induced at 0.8 OD with 0.5 mM IPTG at 37 °C for 3 h. After lysis through tip sonication in lysis buffer (50 mM Tris pH 7.4, 150 mM NaCl, 0.2 mM TCEP), the expressed protein was extracted from the supernatant using NiNTA resin (QIAGEN, Germantown, MD). The resulting eluate from the NiNTA resin using lysis buffer supplemented with 250 mM Imidazole pH 7.4 was loaded onto the Superdex 75 16/60 column (GE Healthcare) for gel filtration. Subsequently, the resulting solution was purified using anion exchange chromatography using 5 mL HiTrap Q HP (Cytiva). Finally, the eluate was loaded on an equilibrated Superdex 75 16/60 column (GE Healthcare), and the protein purity was assessed using sodium dodecyl sulfate-polyacrylamide gel electrophoresis (SDS-PAGE). The concentration of the purified protein was calculated by measuring the absorbance at 280 nm. Finally, the protein was concentrated at approximately 50 μM and stored at −80 °C in small aliquots.

ESCRT-I (TSG101, VPS28, VPS37B, and MVB12A) was expressed in HEK293 cells. ESCRT-I had a Strep-tagged VPS28 subunit and was initially purified on StrepTactin Sepharose (IBA), followed by gel filtration chromatography on a Superdex 200 16/60 column (GE Healthcare), in 50 mM Tris pH 7.4, 300 mM NaCl, 0.1 mM TCEP.

Fluorophore labeling was performed overnight at 4 °C using cysteine reactive dyes on engineered cysteines (A78C for ALG-2 and all its mutants) or native surface-exposed cysteines (ESCRT-I). Specifically, Atto 488 maleimide (Sigma-Aldrich) was used for labeling ALG-2 (and all its mutants) and sulfo-Cy3 maleimide (Fischer Scientific) for labeling ESCRT-I. Excess dye was removed by sequentially passing the protein-dye mixture through two PD10 columns (Cytiva). The final step in every protein purification was gel filtration chromatography to ensure the monodisperse state of the (labeled) protein. Labeling efficiencies were normally around 25% for ALG-2 and all its mutants and >75% for ESCRT-I.

Reconstitution Reactions and Confocal Microscopy. The incubation reactions were set up in a microcentrifuge tube at room temperature before transferring to a Lab-Tek II chambered cover glass (Fisher Scientific) for imaging. The imaging chamber was pre-coated with a 5 mg/mL solution of fatty acid-free Bovine Serum Albumin for 30 min and washed three times with the reaction buffer (25 mM HEPES at pH 7.4, 125 mM NaCl, and 0.2 mM TCEP, 280 mOsm) before transferring the reactants from the microcentrifuge tubes. Then, 15 μL of GUVs were mixed with 120 μL of reaction buffer containing proteins at concentrations stated in the results section. After 15-min incubation images were acquired on a Nikon A1 confocal microscope with a 63× Plan Apochromat 1.4 numerical aperture (NA) objective. Three replicates were performed for each experimental condition in different imaging chambers. Identical laser power and gain settings were used for each set of replicates. The reconstitution experiments were performed within 48 h of GUV preparation to limit the photooxidation of lipids. All experiments were performed at room temperature.

The images for cell experiments were acquired on an Olympus IX83 microscope with a Yokogawa CSU-W1 spinning disk confocal scanner unit, an Olympus PlanApo 60x 1.42 NA objective, and an ImageEMX2 digital camera or Hamamatsu Orca Fusion CMOS digital camera. Images were acquired with Metamorph software version 7.10.3279 (Molecular Devices).

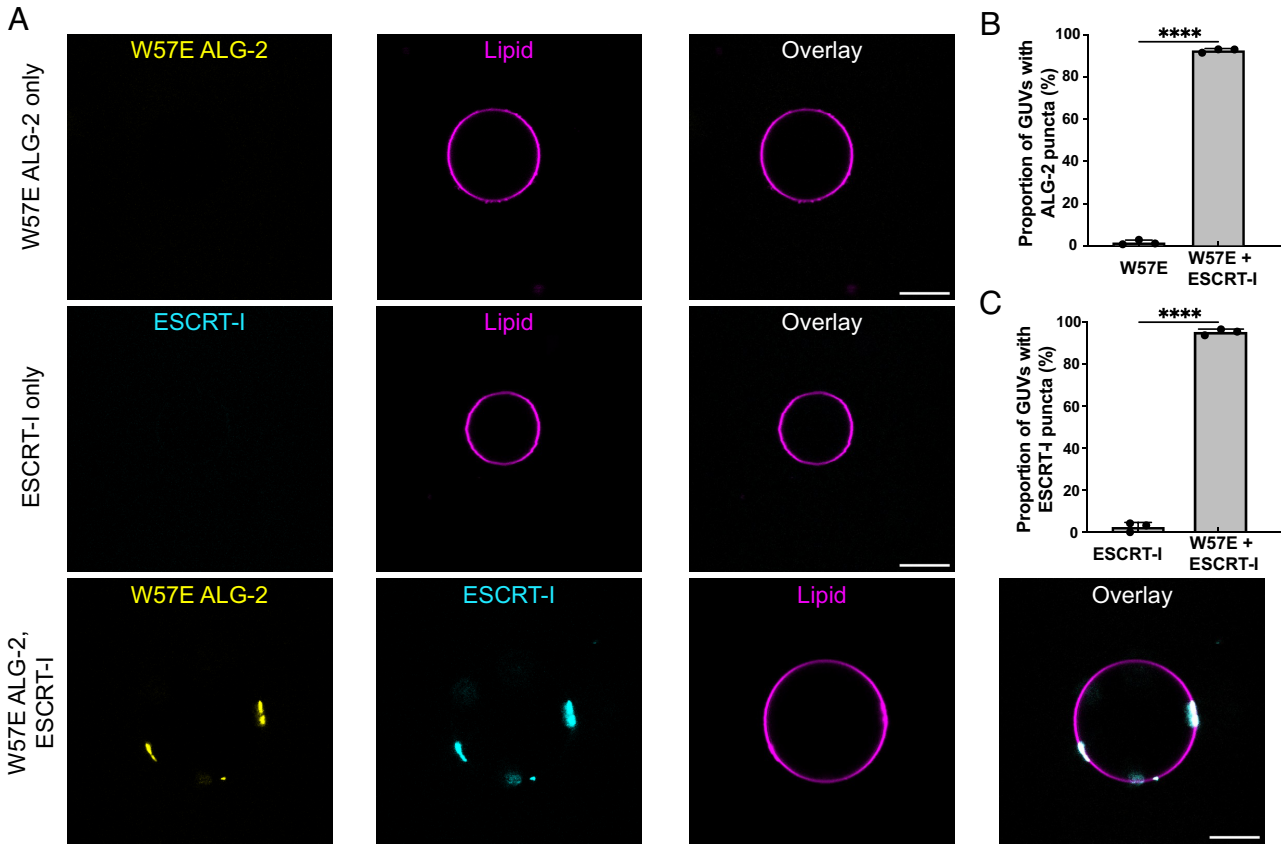

Fig. 5. ESCRT-I rescues the membrane recruitment of ALG-2 mutants. (*A*) (*Top* row) Fluorescently labeled W57E ALG-2 (Atto 488; 200 nM) was mixed with 30% DOPS containing GUVs and imaged. No recruitment of W57E ALG-2 on the membranes was observed. (*Bottom* row) Upon the addition of ESCRT-I (Cy3; 50 nM) to the GUVs incubated with W57E ALG-2 (Atto 488; 200 nM), clear puncta of W57E ALG-2 and ESCRT-I onto the membranes, which also colocalize, are observed. (*B*) The proportion of GUVs that had at least one ALG-2 punctum on their periphery were plotted for fluorescently labeled W57E ALG-2 only (n = 395 GUVs) and W57E ALG-2 with ESCRT-I (n = 332 GUVs). (*C*) shows the proportion of GUVs with ESCRT-I punctum on their periphery with ESCRT-I only (n = 372 GUVs) and ESCRT-I with W57E ALG-2 (n = 332 GUVs). The circles on the bar charts represent independent data points and the data are shown as mean ± SD (vertical line). All results are from at least three independent experiments. $P \leq 0.003$ (***), ns = not significant. (Scale bar, 10 μm.)

Cell Culture. All cells were maintained at 37 °C and supplemented with 5% CO_2. HeLa human cervical adenocarcinoma originally from the American Type Culture Collection (ATCC) were grown in Dulbecco's modified Eagle's medium (DMEM) (no. 11965-084; Gibco) supplemented with 9% v/v fetal bovine serum (FBS; Atlanta Biologicals, S11150).

DNA Transfection. Cells were suspended by trypsinization and transfected using Lipofectamine 2000 (Invitrogen, no. 11668027) according to the manufacturer's instructions.

Live Cell Imaging. Cells were seeded in a four-chamber, no. 1.5 glass-bottom dish (Cellvis) and cultured as appropriate for the intended experiment. Before imaging, the medium was replaced with a warm imaging solution [DMEM, high glucose, HEPES, no phenol red (Gibco, 21063029) supplemented with 10% v/v fetal bovine serum]. The dish was immediately transferred to a Tokai Hit (model: STXG-WSKMX-SET) stage-top incubator preheated to 37 °C. The dish was allowed to equilibrate for 10 min before initiating acquisition.

Immunofluorescence. Cells were fixed in 4% w/v paraformaldehyde in phosphate-buffered saline (PBS) for 15 min at room temperature, rinsed with PBS, and permeabilized in 0.1% v/v Triton X-100 (Pierce Biotechnology). Cells were immunolabeled in blocking solution for 1 h at RT with antibody against Sec31A (Transduction lab, 1:1,000). After rinsing with PBS, goat secondary antibodies conjugated to Alexa Fluor 488 fluorescent dyes (Molecular Probes) were diluted to 1 μg/mL in blocking solution and were added to cells for 45 min.

Image Analysis. Custom-made scripts were used to perform puncta recognition analysis in Python. We started by using Machine learning to train our model [Yolov5 developed by Ultralytics (https://github.com/ultralytics/yolov5.git)] for GUV recognition. Next, we used this trained model to recognize individual GUVs from confocal image frames with multiple GUVs. We used the corresponding protein channels for puncta recognition for each recognized GUV. In each protein channel, we performed background subtraction based on the background intensity determined using minimum cross entropy thresholding (threshold_li from scikit-image). Next, we performed Gaussian noise reduction on the background-subtracted images using the Fast NI Means Denoising algorithm followed by Gaussian Blur to get a regularly shaped punctum. Subsequently, we adjusted the image contrast to sparse out the image pixel values (using Equalize Bar chart from OpenCV) before generating a binary mask (using threshold_otsu from scikit-image, which minimizes the intra-group pixel value variance). In the foreground pixels, we counted groups of connected pixels that are larger than 5 pixels as individual punctum. We calculated the proportion of GUVs with puncta as the ratio of GUVs that have at least one punctum with the total number of recognized GUVs. Finally, for each recognized punctum, we generated a rectangular bounding box. We considered a punctum as colocalized among different protein channels if their bounding boxes overlapped. The proportion of colocalized puncta was calculated as the colocalized punctum divided by the total puncta in the channel with the highest puncta.

The representative images in Figs. 1*B* and 5 were background subtracted before contrast adjustment for clear puncta depiction. Specifically, the representative figures were thresholded to remove the background fluorescence from the unbound fluorescent protein and depict the puncta observed on the periphery of GUVs. For each representative image, a square area of approximately 10 pixels was selected outside the periphery of the GUV in ImageJ. The average pixel value within this selected area was considered the background fluorescence intensity and subtracted from the entire channel. Similar thresholding was done for each (both protein and lipid) channel. Finally, the LUTs for the backgrounded subtracted

channels were marginally adjusted to improve the contrast of the puncta on the GUV periphery. This does not affect our quantification analysis which has been described previously.

All image analyses for cell experiments were performed in ImageJ. To quantify for mCherry-ALG-2 positive area, a threshold was empirically determined for individual cells with different expression levels. ImageJ command *Analyze Particle* was then used to measure above threshold particle area per cell.

MD Simulations. MD simulations were performed with GROMACS 2020 (33) using the CHARMM36m force field (34). Atomistic models of the apo and Ca^{2+}-bound forms of ALG-2 were based on crystal structures with PDB IDs 2ZND and 2ZN9 (15), respectively. Each subunit of the dimeric models consisted of residues 21–191. The N-terminal Gly/Pro-rich region shown to be dispensable for ALG-2 membrane binding in GUV-based experiments was excluded from our structural models. The exposed amino group of Ala21 in the truncated construct was neutralized. Mutant structures were generated in PyMOL (35). Protonation states of amino acid side chains were assigned according to pKa prediction by PROPKA (36). Six 14 × 14 nm^2 patches of membrane each consisting of a random distribution of 70% DOPC and 30% DOPS coarse-grained lipids were independently prepared using the *insane* method (37), solvated with 150 mM of aqueous NaCl, equilibrated for 200 ns, and converted into an atomistic representation using the CG2AT2 tool (38). Atomistic structures of wild-type or mutant ALG-2 were placed above the resulting membranes with a minimum distance of ~2 nm. Each protein–membrane system was subsequently subjected to re-solvation and 10 ns of further equilibration. During equilibration, harmonic positional restraints with a force constant of 1,000 kJ mol^{-1} were applied to non-hydrogen protein atoms or backbone beads. For the Ca^{2+}-bound form of wild-type or mutant ALG-2, harmonic restraints with a force constant of 100 kJ mol^{-1} were additionally applied to the distance between each calcium ion and the center of mass of its coordinating atoms during simulations. The system temperature and pressure were maintained at 310 K and 1 bar, respectively, using the velocity-rescaling thermostat (39) and a semi-isotropic Parrinello-Rahman barostat (40) in the production phase. The integration time step was 2 fs. Long-range electrostatic interactions were treated using the smooth particle mesh Ewald method (41, 42) with a Fourier spacing of 0.12 nm and charge interpolation through fourth-order B-splines. We applied a real-space distance cut-off of 1 nm to non-bonded interactions. The LINCS algorithm was used to constrain covalent bonds involving hydrogen atoms (43). Simulation trajectories were analyzed through MDAnalysis 2.0 (44, 45) in Python 3.6.

Poisson–Boltzmann Calculations. Electrostatic potential maps were calculated for apo and Ca^{2+}-bound ALG-2 by numerically solving the linearized Poisson-Boltzmann equation (46) using the Adaptive Poisson–Boltzmann Solver (47, 48). The multigrid finite-difference calculation (49) was performed on a 129 × 129 × 129 grid with dimensions 13 × 13 × 13 nm^3, applying Debye–Hückel boundary conditions, and the finer grid focused into 10 × 10 × 10 nm^3. Protein atoms were assigned radii and partial charges from the CHARMM36m force field (50). The radius of an implicit solvent molecule was set to 0.14 nm, the ionic strength to that of 0.15 M NaCl, and the dielectric constant to 78.5 for the solvent and 2 for the protein.

Modeling Analysis. AlphaFold2 (https://alphafold.ebi.ac.uk/) was run using the ColabFold notebook (https://colab.research.google.com/github/sokrypton/ColabFold) using version v1.5.2 on default settings. ChimeraX 1.3 was used to overlay the AlphaFold predicted R34E/K37E/R39E ALG-2 with des3–23 WT ALG-2 (PDB–2ZN9) as shown in *SI Appendix*, Fig. S1.

Statistical Analysis. Statistical analysis was performed with GraphPad Prism 9.0. The data of the GUV binding assay were analyzed by Student's *t* test and one-way ANOVA. The significance between the two calculated areas was determined using a Student's two-tailed unpaired *t* test. $P < 0.05$ was considered statistically significant.

Data, Materials, and Software Availability. All study data are included in the article and/or *SI Appendix*.

ACKNOWLEDGMENTS. We thank Liv Jensen for help with data analysis script. This research was supported by Hoffmann-La Roche as part of the Alliance for Therapies in Neuroscience (J.H.H.) and the NIH grants R01 GM122434 (P.I.H.) and F32 AI155226 (K.P.L.). Other unrelated work in the Hurley lab is funded by Genentech.

1. M. Maki, T. Takahara, H. Shibata, Multifaceted roles of ALG-2 in Ca(2+)-regulated membrane trafficking. *Int. J. Mol. Sci.* **17**, 1401 (2016).
2. J. H. Hurley, P. I. Hanson, Membrane budding and scission by the ESCRT machinery: It's all in the neck. *Nat. Rev. Mol. Cell Biol.* **11**, 556–566 (2010).
3. M. Vietri, M. Radulovic, H. Stenmark, The many functions of ESCRTs. *Nat. Rev. Mol. Cell Biol.* **21**, 25–42 (2020).
4. L. L. Scheffer *et al.*, Mechanism of Ca(2)(+)-triggered ESCRT assembly and regulation of cell membrane repair. *Nat. Commun.* **5**, 5646 (2014).
5. M. L. Skowyra, P. H. Schlesinger, T. V. Naismith, P. I. Hanson, Triggered recruitment of ESCRT machinery promotes endolysosomal repair. *Science* **360**, eaar5078 (2018).
6. X. Li *et al.*, A molecular mechanism to regulate lysosome motility for lysosome positioning and tubulation. *Nat. Cell Biol.* **18**, 404–417 (2016).
7. C. A. McGourty *et al.*, Regulation of the CUL3 ubiquitin ligase by a calcium-dependent co-adaptor. *Cell* **167**, 525–538.e514 (2016).
8. J. X. Tan, T. Finkel, A phosphoinositide signalling pathway mediates rapid lysosomal repair. *Nature* **609**, 815–821 (2022).
9. M. Radulovic *et al.*, Cholesterol transfer via endoplasmic reticulum contacts mediates lysosome damage repair. *EMBO J.* **41**, e112677 (2022).
10. J. J. Chen *et al.*, Compromised function of the ESCRT pathway promotes endolysosomal escape of tau seeds and propagation of tau aggregation. *J. Biol. Chem.* **294**, 18952–18966 (2019).
11. J. Jia, S. Tarabykina, C. Hansen, M. Berchtold, M. Cygler, Structure of apoptosis-linked protein ALG-2: Insights into Ca^{2+}-induced changes in penta-EF-hand proteins. *Structure* **9**, 267–275 (2001).
12. A. Yamasaki, K. Tani, A. Yamamoto, N. Kitamura, M. Komada, The Ca^{2+}-binding protein ALG-2 is recruited to endoplasmic reticulum exit sites by Sec31A and stabilizes the localization of Sec31A. *Mol. Biol. Cell* **17**, 4876–4887 (2006).
13. H. Shibata, H. Suzuki, H. Yoshida, M. Maki, ALG-2 directly binds Sec31A and localizes at endoplasmic reticulum exit sites in a Ca^{2+}-dependent manner. *Biochem. Biophys. Res. Commun.* **353**, 756–763 (2007).
14. T. Takahashi *et al.*, Structural analysis of the complex between penta-EF-hand ALG-2 protein and Sec31A peptide reveals a novel target recognition mechanism of ALG-2. *Int. J. Mol. Sci.* **16**, 3677–3699 (2015).
15. H. Suzuki *et al.*, Structural basis for Ca^{2+}-dependent formation of ALG-2/Alix peptide complex: Ca^{2+}/EF3-driven arginine switch mechanism. *Structure* **16**, 1562–1573 (2008).
16. M. A. Swairjo, N. O. Concha, M. A. Kaetzel, J. R. Dedman, B. A. Seaton, Ca(2+)-bridging mechanism and phospholipid head group recognition in the membrane-binding protein annexin V. *Nat. Struct. Biol.* **2**, 968–974 (1995).
17. M. A. Lemmon, Membrane recognition by phospholipid-binding domains. *Nat. Rev. Mol. Cell Biol.* **9**, 99–111 (2008).
18. J. Guillén *et al.*, Structural insights into the Ca^{2+} and $PI(4,5)P_2$ binding modes of the C2 domains of rabphilin 3A and synaptotagmin 1. *Proc. Natl. Acad. Sci. U.S.A.* **110**, 20503–20508 (2013).
19. R. Voleti, D. R. Tomchick, T. C. Südhof, J. Rizo, Exceptionally tight membrane-binding may explain the key role of the synaptotagmin-7 C2A domain in asynchronous neurotransmitter release. *Proc. Natl. Acad. Sci. U.S.A.* **114**, E8518–E8527 (2017).
20. S. Shukla, K. P. Larsen, C. Ou, K. Rose, J. H. Hurley, In vitro reconstitution of calcium-dependent recruitment of the human ESCRT machinery in lysosomal membrane repair. *Proc. Natl. Acad. Sci. U.S.A.* **119**, e2205590119 (2022).
21. J. Jumper *et al.*, Highly accurate protein structure prediction with AlphaFold. *Nature* **596**, 583–589 (2021).
22. M. Maki, S. V. Narayana, K. Hitomi, A growing family of the Ca^{2+}-binding proteins with five EF-hand motifs. *Biochem. J.* **328**, 718–720 (1997).
23. N. Verdaguer, S. Corbalan-Garcia, W. F. Ochoa, I. Fita, J. C. Gómez-Fernández, Ca(2+) bridges the C2 membrane-binding domain of protein kinase Calpha directly to phosphatidylserine. *EMBO J.* **18**, 6329–6338 (1999).
24. Y. Hirano *et al.*, Structural basis of phosphatidylcholine recognition by the C2–domain of cytosolic phospholipase A2α. *eLife* **8**, e44760 (2019).
25. H. Shibata *et al.*, The ALG-2 binding site in Sec31A influences the retention kinetics of Sec31A at the endoplasmic reticulum exit sites as revealed by live-cell time-lapse imaging. *Biosci. Biotechnol. Biochem.* **74**, 1819–1826 (2010).
26. J. M. la Cour, A. J. Schindler, M. W. Berchtold, R. Schekman, ALG-2 attenuates COPII budding in vitro and stabilizes the Sec23/Sec31A complex. *PLoS ONE* **8**, e75309 (2013).
27. W. Chen, M. M. Motsinger, J. Li, K. P. Bohannon, P. I. Hanson, Ca2+-sensor ALG-2 engages ESCRTs to enhance lysosomal membrane resilience to osmotic stress. bioRxiv [Preprint] (2024). https://doi.org/10.1101/2024.02.04.578682 (Accessed 4 February 2024).
28. E. Boura, J. H. Hurley, Structural basis for membrane targeting by the MVB12–associated β-prism domain of the human ESCRT-I MVB12 subunit. *Proc. Natl. Acad. Sci. U.S.A.* **109**, 1901–1906 (2012).
29. G. van Meer, D. R. Voelker, G. W. Feigenson, Membrane lipids: where they are and how they behave. *Nat. Rev. Mol. Cell Biol.* **9**, 112–124 (2008).
30. J. Jacquemyn, A. Cascalho, R. E. Goodchild, The ins and outs of endoplasmic reticulum-controlled lipid biosynthesis. *EMBO Rep.* **18**, 1905–1921 (2017).
31. D. Casares, P. V. Escribá, C. A. Rosselló, Membrane lipid composition: Effect on membrane and organelle structure, function and compartmentalization and therapeutic avenues. *Int. J. Mol. Sci.* **20**, 2167 (2019).
32. A. Weinberger *et al.*, Gel-assisted formation of giant unilamellar vesicles. *Biophys. J.* **105**, 154–164 (2013).
33. M. J. Abraham *et al.*, GROMACS: High performance molecular simulations through multi-level parallelism from laptops to supercomputers. *SoftwareX* **1–2**, 19–25 (2015).

34. J. Huang *et al.*, CHARMM36m: An improved force field for folded and intrinsically disordered proteins. *Nat. Methods* **14**, 71–73 (2017).
35. W. L. Delano, PyMOL: An open-source molecular graphics tool. *CCP4 Newsl. Protein Crystallogr.* **40**, 82–92 (2002).
36. M. H. M. Olsson, C. R. Søndergaard, M. Rostkowski, J. H. Jensen, PROPKA3: Consistent treatment of internal and surface residues in empirical pKa predictions. *J. Chem. Theory Comput.* **7**, 525–537 (2011).
37. T. A. Wassenaar, H. I. Ingólfsson, R. A. Böckmann, D. P. Tieleman, S. J. Marrink, Computational lipidomics with insane: A versatile tool for generating custom membranes for molecular simulations. *J. Chem. Theory Comput.* **11**, 2144–2155 (2015).
38. O. N. Vickery, P. J. Stansfeld, CG2AT2: An enhanced fragment-based approach for serial multi-scale molecular dynamics simulations. *J. Chem. Theory Comput.* **17**, 6472–6482 (2021).
39. G. Bussi, D. Donadio, M. Parrinello, Canonical sampling through velocity rescaling. *J. Chem. Phys.* **126**, 014101 (2007).
40. M. Parrinello, A. Rahman, Polymorphic transitions in single crystals: A new molecular dynamics method. *J. Appl. Phys.* **52**, 7182–7190 (1981).
41. T. Darden, D. York, L. Pedersen, Particle mesh Ewald: An N·log(N) method for Ewald sums in large systems. *J. Chem. Phys.* **98**, 10089–10092 (1998).
42. U. Essmann *et al.*, A smooth particle mesh Ewald method. *J. Chem. Phys.* **103**, 8577–8593 (1995).
43. B. Hess, H. Bekker, H. J. C. Berendsen, J. G. E. M. Fraaije, LINCS: A linear constraint solver for molecular simulations. *J. Comput. Chem.* **18**, 1463–1472 (1997).
44. N. Michaud-Agrawal, E. J. Denning, T. B. Woolf, O. Beckstein, MDAnalysis: A toolkit for the analysis of molecular dynamics simulations. *J. Comput. Chem.* **32**, 2319–2327 (2011).
45. R. Gowers *et al.*, *MDAnalysis: A Python Package for the Rapid Analysis of Molecular Dynamics Simulations*, S. Benthall, S. Rostrup (SciPy, 2016), pp. 98–105.
46. M. E. Davis, J. A. McCammon, Electrostatics in biomolecular structure and dynamics. *Chem. Rev.* **90**, 509–521 (1990).
47. N. A. Baker, D. Sept, S. Joseph, M. J. Holst, J. A. McCammon, Electrostatics of nanosystems: Application to microtubules and the ribosome. *Proc. Natl. Acad. Sci. U.S.A.* **98**, 10037–10041 (2001).
48. E. Jurrus *et al.*, Improvements to the APBS biomolecular solvation software suite. *Protein Science* **27**, 112–128 (2018).
49. M. K. Gilson, B. H. Honig, Calculation of electrostatic potentials in an enzyme active site. *Nature* **330**, 84–86 (1987).
50. J. Huang *et al.*, CHARMM36m: An improved force field for folded and intrinsically disordered proteins. *Nat. Methods* **14**, 71–73 (2016).